3.4 % solar-to-ammonia efficiency from nitrate using Fe single atomic catalyst supported on MoS2 nanosheets

Ji Li

College of Bioresources and Materials Engineering, Shaanxi University of Science & Technology

Yuan Zhang

College of Bioresources and Materials Engineering, Shaanxi University of Science & Technology

Chao Liu

Shaanxi Collaborative Innovation Center of Industrial Auxiliary Chemistry and Technology, Shaanxi University of Science and Technology

Li Rong Zheng

Chinese Academy of Sciences

Eddy Petit

Institut Europeen des Membranes, IEM, UMR 5635, Université Montpellier, ENSCM, CNRS

Kun Qi

Institut Europ&#x00E9   https://orcid.org/0000-0002-5574-4475

Yang Zhang

Institut Europeen des Membranes, IEM, UMR 5635, Université Montpellier, ENSCM, CNRS

Huali Wu

Institut Europeen des Membranes, IEM, UMR 5635, Université Montpellier, ENSCM, CNRS

Wensen Wang

Institut Europeen des Membranes, IEM, UMR 5635, Université Montpellier, ENSCM, CNRS

Antoine Tiberj

Laboratoire Charles Coulomb (L2C), Université de Montpellier, CNRS   https://orcid.org/0000-0002-8609-3986

Xuechuan Wang

College of Bioresources and Materials Engineering, Shaanxi University of Science & Technology

Manish Chhowalla

University of Cambridge   https://orcid.org/0000-0002-8183-4044

Luc Lajaunie

Departamento de Ciencia de los Materiales e Ingeniería Metalúrgica y Química Inorgánica, Facultad de Ciencias, Universidad de Cádiz   https://orcid.org/0000-0001-6152-6784

Ruohan Yu

Wuhan University of Technology

Damien Voiry (✉ damien.voiry@umontpellier.fr)

Institut Europeen des Membranes, IEM, UMR 5635, Université Montpellier, ENSCM, CNRS

Article

3.4 % solar-to-ammonia efficiency from nitrate using Fe single atomic catalyst supported on MoS₂ nanosheets

Ji Li,[a,b] Yuan Zhang,[a] Chao Liu,[c] Lirong Zheng,[d] Eddy Petit,[b] Kun Qi,[b] Yang Zhang,[b] Huali Wu,[b] Wensen Wang,[b] Antoine Tiberj,[e] Xuechuan Wang,[a] Manish Chhowalla,[f] Luc Lajaunie,[g,h] Ruohan Yu,[i] Damien Voiry [b,*]

a College of Bioresources and Materials Engineering, Shaanxi University of Science & Technology, Xi'an 710021, PR China

b Institut Europeen des Membranes, IEM, UMR 5635, Université Montpellier, ENSCM, CNRS, 34095 Montpellier Cedex 5, France

c Shaanxi Collaborative Innovation Center of Industrial Auxiliary Chemistry and Technology, Shaanxi University of Science and Technology, Xi'an 710021, PR China

d Institute of High Energy Physics, Chinese Academy of Science, Beijing 100049, PR China

e Laboratoire Charles Coulomb (L2C),Université de Montpellier, CNRS, Montpellier, 34095, France

f Department of Materials Science & Metallurgy, University of Cambridge, Cambridge, UK

g Departamento de Ciencia de los Materiales e Ingeniería Metalúrgica y Química Inorgánica, Facultad de Ciencias, Universidad de Cádiz, Campus Río San Pedro S/N, Puerto Real, 11510, Cádiz, Spain

h Instituto Universitario de Investigación de Microscopía Electrónica y Materiales (IMEYMAT), Facultad de Ciencias, Universidad de Cádiz, Campus Río San Pedro S/N, Puerto Real 11510, Cádiz, Spain

i Nanostructure Research Centre (NRC), Wuhan University of Technology, Wuhan 430070, PR China

* Corresponding author: Damien. Voiry(damien.voiry@umontpellier.fr)

ABSTRACT

Electrochemical synthesis of NH_3 is a carbon-free alternative to the traditional Haber-Bosch process. The challenge with nitrogen reduction reaction (NRR) to NH_3 is cleavage of the inert $N{\equiv}N$ triple bond of nitrogen gas. Obtaining NH_3 from environmental pollutants, such as nitrates or nitrites, is a more practical route than NRR. However, reduction of nitrates or nitrites to ammonia is currently hampered by modest Faradaic efficiencies, typically below 10 %. Here, we report a novel heterogeneous catalyst based on iron (Fe) single-atoms supported on two-dimensional MoS_2 (Fe-MoS_2) for the nitrate reduction reaction (NO_3RR). We have found that Fe-MoS_2 exhibits remarkable performance with a maximum Faradaic efficiency of 98 % for NO_3RR to NH_3 at an overpotential of -0.48 V vs. the reversible hydrogen electrode (RHE) as confirmed by our isotopic nuclear magnetic resonance (NMR) analyses. Density function theory (DFT) calculations reveal that the enhanced selectivity for the production of NH_3 from single Fe atoms supported on MoS_2 is attributed to a reduced energy barrier of 0.38 eV associated with de-oxidation of *NO to *N – the usual potential limiting step in NO_3RR. We assembled our catalyst in a two-electrode electrolyzer coupled to an InGaP/GaAs/Ge triple-junction solar cell to demonstrate a solar-to-ammonia (STA) conversion efficiency of 3.4 % and a yield rate of 0.03 mmol h^{-1} cm^{-2} equivalent to 510 µg h^{-1} cm^{-2}. Our results open new avenues for design of single-atom catalysts (SAC) for the realization of solar-driven ammonia production.

49

50   **MAIN TEXT**

51   Ammonia (NH_3) is an important industrial chemical that is widely applied as a nitrogen-

52   rich fertilizer for agriculture, textiles, plastics, and the pharmaceutical industry.[1,2] The N cycle

53   perturbation is among the 3 identified planetary boundaries that have already been transgressed

54   by humanity.[3] For renewable energy and net-zero carbon emission, ammonia has been

55   identified as a promising energy carrier because of its high hydrogen content of 17.7 wt % and

56   its high gravimetric energy density at 3 kWh kg^{-1}.[4–7] The synthesis of NH_3 via the Haber-Bosch

57   reaction is done under harsh conditions with temperatures and pressures exceeding 400 °C and

58   200 bar, respectively. With an annual production of 250×10^6 tons, an estimated amount of 1%

59   of the world's energy is utilized in the Haber-Bosch, which is responsible for 1.4 % of the global

60   carbon dioxide emissions.[8–10] As an alternative, the use of nitrogen and water for the electro-

61   catalytic synthesis of ammonia has recently attracted widespread attention.[11,12] However, the

62   direct electrochemical reduction of N_2 for the production of ammonia under mild conditions is

63   severely limited by several bottlenecks such as: *i*) the high energy barrier required for cleavage

64   of inert N≡N triple bond;[13,14] *ii*) nonpolar nature of nitrogen molecules that results in a weak

65   interaction between N_2 and active sites of catalysts;[15] *iii*) the very low solubility of N_2 in water

66   leading to slow reaction rates.[16,17]

67   Alternatively, nitrates (NO_3^-) possess unique advantages as nitrogen sources for

68   electrosynthesis of NH_3. The bond energy of polar N=O (204 kJ/mol) is four times weaker than

69   the inert non-polar N≡N triple bond, and therefore the N=O bond can be easily activated at

70   lower energies.[18] Nitrate is widely present in the environment and accumulates over time due

71   to agriculture and industrial production activity.[19,20] NO_3^- is a common pollutant of water

72   resources that is responsible for birth defects such as infant methemoglobinemia and blue-baby

73   syndrome as well as thyroid and bladder cancers. NO₃RR for NH_3 production is therefore not

74 only in line with energy sustainability but is also a pollution mitigation strategy. The

75 electrocatalytic reduction of NO_3^--to-NH$_3$ has been reported using Fe,[21] Al,[21] Cu bulk and

76 nanorods,[22,23] Cu$_2$O/Cu wires,[24] Cu-Ni alloys,[25] Cu molecular catalyst,[17] Co$_3$O$_4$,[26–29] and

77 carbon-based materials.[30,31] However, most NO$_3$R reactions typically suffer from modest

78 Faradaic efficiencies and/or stability.

79   We have recently identified chemically exfoliated MoS$_2$ nanosheets as two-dimensional

80 electrocatalysts for efficient oxidation of organic sulfides to sulfoxides with near-unity

81 selectivity.[32] The nitrate reductase enzyme possesses a Mo (IV) active site coordinated with

82 sulfur coordinating ligands similar to the dimethyl sulfoxide (DMSO) reductase, whereas the

83 nitrogenase is a multinuclear enzyme with MoFe$_7$ clusters as the active sites. Fe-based catalysts

84 have been reported to be promising for NO$_3$RR but the Faradaic efficiency is low because of

85 the competing hydrogen evolution reaction and the formation of nitrogen *via* the five-electron

86 transfer pathway.[33–35] To improve the selectivity to NO_3^--to-NH$_3$, Fe single-atom catalysts

87 (SACs) hold promise because the individual Fe atoms possess coordination environment that

88 results in efficient catalytic activity compared to bulk and nanostructured iron. To date, Fe-

89 SACs have been used in various heterogeneous catalytic reactions, such as CO oxidation,[36]

90 oxygen reduction reaction (ORR),[37–39] CO$_2$ reduction reaction (CO$_2$RR),[40,41] and nitrogen

91 reduction reaction (NRR).[42,43]

92   Inspired by the structure of active sites of enzymes, we report SACs based on individual

93 Fe atoms supported on MoS$_2$ nanosheets (Fe-MoS$_2$) for the electrocatalytic NO$_3$RR, which

94 exhibits excellent performance with a Faradaic efficiency of 98 % toward NH$_3$ at a low

95 overpotential of -0.48 V versus the reversible hydrogen electrode (*vs*. RHE) and a cathodic

96 energy efficiency of 31% at *vs*. RHE and -0.28 V *vs*. RHE, respectively. The optimized Fe-

97 MoS$_2$ SACs were implemented in a 2-electrode electrolyzer coupled to an external photovoltaic

98 (PV) device to allow solar-driven conversion of NO_3^- to NH$_3$ to demonstrate a maximum yield

99   rate of 0.03 μmol h^{-1} cm^{-2} equivalent to 510 μg h^{-1} with a near-unity FE for NH$_3$. The system

100 delivers stable ammonia production and we estimated the solar-to-ammonia (STA) conversion

101 efficiency to be ca. 3.4 % – setting a new benchmark for the production of NH$_3$ from a PV-

102 powered electrolyzer.

103

104 **Synthesis and characterization of the Fe-MoS$_2$ SAC**

105   MoS$_2$ and Fe-MoS$_2$ nanosheets were synthesized *via* a hydrothermal reaction using

106 ammonium tetrathiomolybdate: (NH$_4$)$_2$MoS$_4$ and iron(III) nitrate nonahydrate as precursors of

107 MoS$_2$ and Fe, respectively.[44] The morphology of as-synthesized Fe-MoS$_2$ was characterized by

108 scanning electron microscopy (SEM) and transmission electron microscopy (TEM). SEM

109 revealed the 2D of the MoS$_2$ nanosheets (**Figure 1a**), cross-sectional TEM revealed the uniform

110 coverage of the MoS$_2$ nanosheets film (thickness ~150 nm) on the conducting carbon cloth

111 (**Figure 1b**). The HAADF-STEM analysis of single-layer catalyst regions shows that the

112 nanosheets are highly crystalline as evidenced by the fast Fourier transform (FFT) patterns in

113 **Figure 1c** and **Supplementary Figure 1**. The observation along [110] direction of the MoS$_2$

114 slabs reveal the presence of the 1T polytype in Fe-MoS$_2$ in agreement with the presence of *J*

115 peaks in the Raman spectra (**Supplementary Figure 2**). Energy-dispersive X-ray spectroscopy

116 (EDS) elemental mapping was used to confirm the presence of Fe on MoS$_2$. **Figure 1d,e** show

117 uniform distribution of Fe atoms on the nanosheets and no sign of aggregation was observed

118 even at the highest magnification (**Supplementary Figure 3**). The presence of Fe is also

119 highlighted by spatially-resolved electron energy loss spectroscopy (SR-EELS, **Figure 1f** and

120 **Supplementary Figure 4**). In particular, the EELS chemical maps evidence that the domain

121 size of Fe is equal or below the EELS voxel size (0.16 nm). It should be noted that the presence

122 of oxygen is also highlighted by EELS and will be discussed later. The high-resolution TEM

123 (HR-TEM) images pointed out that Fe-MoS$_2$ retains the layered structure of MoS$_2$ with an

124 interlayer distance of $\approx$ 9.1 Å, ascribed to the (002) crystalline plane (**Figure 1g**). Compared

125 with pristine MoS_2, the interlayer distance is $\sim$ 2.8 Å larger in the present samples, which is

126 attributed to the presence of Fe atoms on the surface of the nanosheets (**Figure 1g** and

127 **Supplementary Figure 5**). This observation is further corroborated by our X-ray diffraction

128 (XRD) analyses in which the d-spacing of $Fe-MoS_2$ was found to be 9.8 Å, which is larger than

129 that of MoS_2 at 6.5 Å (**Figure 1h**). We studied the influence of Fe atoms on interlayer spacing

130 by preparing $Fe-MoS_2$ catalysts with increasing loadings from 1.36 % to 2.14 % (see

131 Supplementary Information for details). The position of the (002) did not change significantly

132 with the Fe: Mo ratio suggesting a similar average d-space for all $Fe-MoS_2$ samples.

133 Interestingly the half maximum (FWHM) decreases with the Fe content whereas the intensity

134 of the (002) peak increases; indicating improved stacking order and crystallinity of the MoS_2

135 nanosheets at higher Fe loadings.[45]

136 Next, we used X-ray photoelectron spectroscopy (XPS) to elucidate the chemical

137 composition of the MoS_2 and $Fe-MoS_2$ catalysts. The Fe2p spectra of $Fe-MoS_2$ unambiguously

138 revealed the presence of Fe on the samples. The spectra can be decomposed into two doublets

139 at 707.9/720.8 eV and 709.6/723.2 eV, which are ascribed to contributions from Fe bonded to

140 S and the satellite peaks, respectively (**Figure 1i**).[46,47] The splitting of the S2p and Mo3d spectra

141 (**Supplementary Figure 6a, b**) for both MoS_2 and $Fe-MoS_2$ suggests the coexistence of the 1T

142 and the 2H phase MoS_2 in agreement with our Raman and STEM analyses. From the

143 deconvolution of the Mo3d and S2p signals, the amount of 1T phase in MoS_2 and $Fe-MoS_2$ is

144 estimated to be 42.5 % and 47.0 % respectively, whereas minimal amount of Mo^{6+} is detected

145 at 16.9 % and 10.2 %. The presence of an additional doublet at 162.6 eV and 163.9 eV was also

146 identified in the S2p region and attributed to S2p1/2 and S2p2/3 signals from S-Fe bond.[48–50]

147 X-ray absorption near-edge spectroscopy (XANES) and extended X-ray absorption fine

148 structure (EXAFS) were acquired to elucidate the electronic and coordination structure of Fe-

MoS$_2$. **Figure 1j** shows the Fe K-edge XANES profiles for Fe-MoS$_2$, compared to that of Fe$_2$O$_3$, FeS, and Fe metal used as references for Fe^{3+}, Fe^{2+}, and Fe^0, respectively. The near-edge absorption energy position of Fe-MoS$_2$ was found to be between that of FeS and Fe$_2$O$_3$, suggesting that the oxidation state of Fe in Fe-MoS$_2$ is comprised of between +2 and +3. Only one main peak was visible at 1.78 Å in the Fourier transformed EXAFS (FT-EXAFS) spectrum of Fe-MoS$_2$ (**Figure 1k**), which is close to that of Fe-S in FeS at 1.87 Å and is attributed to the first coordination shell of Fe-S. It should be noted that no contribution for the Fe-Fe bond expected at ~2.20 Å and ~2.58 Å for Fe^0 and Fe^{3+} in Fe metal and Fe$_2$O$_3$ were observed from the FT-EXAFS spectrum. Our X-ray absorption data suggest the fact that Fe is dispersed on the MoS$_2$ nanosheets at the atomic level. To gain more information on the structural parameters, we performed least-square EXAFS fittings on Fe-MoS$_2$ (see **Supplementary Figure 7** and **Supplementary Table 1**). The corresponding coordination number of Fe atom in the Fe-MoS$_2$ was estimated to be $\approx$ 3.5 with the bond lengths of 2.25 Å and 1.97 Å for Fe-S and Fe-O respectively. The identification of the Fe-O bond may be attributed to the presence of axial oxygen atoms bonded to Fe, in good agreement with the observed spatial overlapping of the Fe and O EELS chemical maps (**Supplementary Figure 4**). All the above results corroborate the single atomic nature of Fe in Fe-MoS$_2$ catalysts as illustrated in **Figure 1l.**

Investigations of the catalytic activity on Fe-MoS$_2$

The electrocatalytic properties of Fe-MoS$_2$ catalyst for the reduction of NO_3^- were investigated in an H-cell reactor using a 0.1 M of K$_2$SO$_4$ + 0.1 M NaOH electrolyte solution (See the Methods section for details about the electrochemical measurements). **Figure 2a** shows linear sweep voltammetry (LSV) curves measured with and without 0.1 M NaNO$_3$ for MoS$_2$, and Fe-MoS$_2$ nanosheets compared to results from carbon support used as reference. Higher current density and lower onset potential were detected in the presence of NO_3^-. To prove that the change in current density originates from the reduction of NO_3^- to NH$_3$ rather than a change

174   in the electrolyte concentration, we estimated the concentration of ammonia after the reaction

175   *via* a colorimetric method using the indophenol blue method (See details in the Supplementary

176   Information file and **Supplementary Figure 8**). Ammonia concentrations were detected in the

177   range of 0.6~2.0 mM after 1 hour of electrolysis under a constant applied potential of -0.48 V

178   versus the reversible hydrogen electrode (*vs.* RHE), which indicates that the change in the LSV

179   data originates from electrocatalytic conversion of NO_3^-. To exclude contamination that could

180   lead to overestimation of ammonia production, isotopic experiments were conducted using 0.1

181   M $Na^{14}NO_3$ and 0.1 M $Na^{15}NO_3$. The ^1H nuclear magnetic resonance (NMR) spectra of the

182   electrolyte after electrolysis are shown in **Figure 2b**. In the case of $Na^{15}NO_3$ electrolyte solution,

183   the ^1H NMR spectrum exhibits two clear symmetric signals at δ = 7.02 and 7.14 ppm with a

184   spacing of 73.1 Hz assigned to $^{15}NH_3$, due to scalar interaction between ^1H and ^{15}N. Conversely,

185   in presence of $Na^{14}NO_3$ three symmetric signals located at 6.99, 7.08, and 7.17 ppm were

186   detected with a spacing of 52.2 Hz ascribed to $^{14}NH_3$.[12] We performed a blank experiment in

187   the absence of NO_3^- and no signals from $^{15}NH_3$ nor $^{14}NH_3$ were detected. Overall, our results

188   confirmed the successful reduction of NO_3^- to NH_3 and rule out contamination. The content of

189   ammonia in the electrolyte was further quantified *via* ^1H NMR using an external standard for

190   calibration (**Supplementary Figure 9**). The ammonia quantification using ^1H NMR and

191   colorimetry are comparable and validates our colorimetric strategy for the quantification of the

192   Faradaic efficiency of the reaction on Fe-MoS$_2$ (**Supplementary Table 3**). **Figure 2c** shows

193   the Faradaic efficiency for the formation of NH_3 on Fe-MoS$_2$ compared to pristine MoS$_2$, Cu,

194   and Cu$_{50}$Ni$_{50}$ alloy used as the benchmarked catalyst for the NO$_3$RR (Ref. [22]). The selectivity

195   of Fe-MoS$_2$ nanosheets rapidly increases with the onset potential and the Faradaic efficiency

196   for NH_3 reaches a maximum value of 95.8% at -0.48 V *vs.* RHE, which is higher than that for

197   MoS$_2$ nanosheets and Cu at 40.8 % and 22.5 % respectively. The enhanced FE on Fe-MoS$_2$

198   translates to a specific current density j_{NH3} of -8.4 mA cm^{-2}, which represents 7.1- and 2.8-fold

199 increase compared to MoS$_2$ and Cu, respectively. The onset potential for NO$_3$RR – measured

200 at -1 mA cm^{-2} – was found to be ≈ 100 mV vs. RHE for Fe-MoS$_2$ compared to 200 mV vs. RHE

201 for Cu (**Figure 2d**). The j_{NH3} and onset potential on Fe-MoS$_2$ are comparable with those from

202 Cu$_{50}$Ni$_{50}$ alloy. To further quantify the catalytic properties of Fe-MoS$_2$, we estimated the

203 cathodic energy efficiency (EE_{NO_3RR}) of the different catalysts. The EE_{NO_3RR} for Fe-MoS$_2$ was

204 found to be the highest at 31 % for a cathodic potential of -0.28 V *vs.* RHE, which is at least 4

205 times higher than that of MoS$_2$, Cu, and Cu$_{50}$Ni$_{50}$ alloy (**Figure 3b**). These results also

206 compared favorably with previous reports from the literature based on CuNi alloy,[51] Cu

207 nanosheets,[52] Cu/CuO nanowire arrays,[53] titanium electrode,[54] and copper-molecular solid

208 catalyst (**Supplementary Table 5**),[55] and other MoS$_2$-based catalysts those we synthesized

209 (**Supplementary Figure 10**). Our investigations indicate that the presence of atomically

210 dispersed Fe on the two-dimensional MoS$_2$ matrix enhances both the intrinsic catalytic activity

211 and the selectivity with respect to H$_2$.

212 We then sought to better understand the behavior of Fe-MoS$_2$ by exploring the influence

213 of Fe loading and the nitrate concentration in the electrolyte. At -0.48 V *vs.* RHE, the Faradaic

214 efficiency continuously increases from 30.1 % up to 95.8 % as the Fe content is increased from

215 0 % (i.e. pristine MoS$_2$) to 2.13% (**Supplementary Figure 11a,b**). The effect of nitrate

216 concentration on catalytic properties was explored by varying the NO_3^- concentration from 10

217 mM up to 100 mM. Remarkably we observed that the FE for NH$_3$ on Fe-MoS$_2$ is largely

218 maintained in presence of diluted NO_3^- and the FE remains as high as 70% for a nitrate

219 concentration as low as 10 mM. On the contrary, the concentration profoundly affects the

220 NO$_3$RR performance of MoS$_2$ and the FE decreases to ~3.8 % for a nitrate concentration of 10

221 mM (**Figure 2e**). This apparent 18-fold increase of FE_{NH_3} in dilute medium highlights the high

222 selectivity of Fe-MoS$_2$ towards the NO$_3$RR versus the competing hydrogen evolution reaction

223 (HER).

224   We assessed the charge transfer resistance (R_{CT}) at the interface between Fe-MoS$_2$ and

225   the electrolyte using electrochemical impedance spectroscopy (EIS) (**Supplementary Figure**

226   **12a**). The Nyquist plots of different catalysts exhibit the typical semicircle shape, which reflects

227   the interface resistance on the electrode surface. By modeling the EIS responses with the

228   Randles equivalent circuit, the values of R_{CT} are found to be low in the case of Fe-MoS$_2$ at 13.1

229   Ω compared to 24.8 Ω for MoS$_2$ and 9.8 Ω for Cu. This points to faster kinetics for electron

230   transfer at the surface of the catalyst in agreement with the reduction of the Tafel slope at 260

231   mV dec^{-1} compared to >500 mV dec^{-1} for pristine MoS$_2$ and other Cu-based catalysts

232   (**Supplementary Figure 12b**). We conclude that the reduced R_{CT} and Tafel slope result from

233   improved conductivity of the Fe-MoS$_2$ nanosheets and the presence of the metallic 1T polytype

234   within the MoS$_2$ lattice. To evaluate the stability toward the conversion of NO_3^- to NH$_3$, we

235   applied a steady-state potential on the Fe-MoS$_2$ electrode, while recording the current density

236   and measuring the FE using colorimetry. **Figure 2f** shows that the FE at -0.48 V *vs.* RHE

237   displays minimal changes over 7 hours with an average value of 98 %. The robustness of the

238   Fe-MoS$_2$ performance was further corroborated by the high retention of the current density,

239   showing that the 7-hour average of yield rate was 431.8±38.6 μg h^{-1} cm^{-2}.

240   We explored the isotopic effect on the NO$_3$RR by investigating the electrochemical

241   responses of Fe-MoS$_2$ in presence of Na^{14}NO$_3$ and Na^{15}NO$_3$ respectively.[56] Using Na^{15}NO$_3$, we

242   observe a decrease in the current density together with an increase of the overpotential of ~40

243   mV (**Figure 3a**). The LSV and chronoamperometry responses were recorded for each nitrate

244   isotope with increasing temperatures from 25 °C to 65 °C and the apparent activation energies

245   were obtained by fitting the *Arrhenius* plot of the specific current density j_{NH3} as a function of

246   T^{-1} (**Figure 3a**). The slope of the *Arrhenius* plot was estimated to be 0.18 and 0.21 for Na^{14}NO$_3$

247   and Na^{15}NO$_3$ respectively. The apparent difference between the two isotopes is in agreement

248   with the change in the polarization curves and is attributed to the slow diffusion of $Na^{15}NO_3$ in

249   the Helmholtz layer as well as in the interlayer of Fe-MoS$_2$ nanosheets.

250   To obtain more insight into the remarkable selectivity of the Fe-MoS$_2$ for the

251   electrosynthesis of NH$_3$, we investigated NO$_3$RR on different MoS$_2$-based SACs with different

252   transition metals. **Supplementary Figure 13** shows the polarization curves on Co-MoS$_2$, Ni-

253   MoS$_2$, Cu-MoS$_2$, and Fe-MoS$_2$ nanosheets in the presence of NO_3^-. Fe-MoS$_2$ outperformed the

254   other MoS$_2$ SACs as evidenced by the larger current density and the lower onset potential

255   compared to Co-MoS$_2$, Ni-MoS$_2$, Cu-MoS$_2$. The FE for NH$_3$ was found to be 59.6 % at -0.3 V

256   *vs*. RHE on Co-MoS$_2$, which is lower than that of Fe-MoS$_2$ at 86.4 % (**Figure 3c**). Remarkably

257   the values of the onset potential for NO$_3$RR and j_{NH3} on Fe-MoS$_2$ are also 4~10 folds higher

258   and at least 400 mV *vs*. RHE lower than other MoS$_2$ catalysts (**Figure 3d**) – strongly suggesting

259   that the dispersed Fe atoms on the MoS$_2$ nanosheets are key for enhancing the intrinsic catalytic

260   activity and selectivity towards the NO$_3$RR.

261

262   **Computational investigations of the NO$_3$RR on MoS$_2$-based SACs**

263   To rationalize our experimental results, we conducted density functional theory

264   calculations to investigate the NO$_3$RR on the different single-atom catalysts supported on MoS$_2$.

265   The structural models of SACs consisted of four different transition metals: Fe, Co, Ni, and Cu

266   atoms coordinated with 3 sulfur atoms as presented in **Supplementary Figure 14**.[57] **Figure 4a**

267   shows the successive steps associated with nitrate reduction on the MoS$_2$ SACs, which can be

268   decomposed into two main electrochemical processes: *NO$_3$$^-$ → *NO$_2$ → *NO →*N and *NH

269   → *NH$_2$ → *NH$_3$ corresponding to the deoxidation and hydrogenation mechanisms,

270   respectively.[23,58] There is a general agreement that the catalytic active sites of MoS$_2$ are located

271   at the edges of the nanosheets.[59] We first computed the Gibbs free energy of the full NO$_3$RR

272   pathway on different MoS$_2$ SACs. On pristine MoS$_2$, the first deoxidation step: *NO$_3$$^-$ → *NO$_2$

is considered as the potential-dependent step (PDS) with a very high reaction free energy of 1.47 eV. Such a high value is attributed to the formation of strong covalent bonds between two adjacent Mo atoms and two oxygen atoms of NO_3^- (with ΔE_{NO3^-} = -4.04 eV for the largest charge transfer of 0.85 e$^-$) (**Supplementary Figure 15**). Conversely, all SACs display a different energy profile illustrating that the inclusion of metallic single atoms profoundly modifies the thermodynamics landscape of the NO$_3$RR on MoS$_2$. The PDS step is associated with the *NO deoxidation step. Among the different metal single atoms, the lowest reaction free energy is obtained for Fe-MoS$_2$ at 0.38 eV – in qualitative agreement with our experimental observations. When plotting the energy barrier for the reaction as function of the experimental onset potential, we observed a linear relationship, which clearly suggests that the catalytic activity of MoS$_2$ SACs is controlled by the barrier of the deoxidation step (**Figure 4d**).

To elucidate the origin of the reduced energy barrier for the PDS on the active sites, we examined the projected densities of states (PDOS) of NO adsorption on Fe-MoS$_2$ (**Supplementary Figure 16**). We found that there is a strong overlap between energy levels of the α-spin and β-spin d orbitals of Fe-MoS$_2$ and the π* orbitals of NO, which leads to an orbital splitting and rearrangement to form new d-π* bonding and antibonding orbitals (**Figure 4b**). According to our calculations of the adsorption energy of *NO on the MoS$_2$ SACs ($E_{ads, NO}$), we identified the following trend: $E_{ads, NO}$(Fe-MoS$_2$)> $E_{ads, NO}$(Co-MoS$_2$)> $E_{ads, NO}$(Ni-MoS$_2$)> $E_{ads, NO}$(Cu-MoS$_2$) (**Supplementary Figure 17** and **Supplementary Table 6**). Our results suggest that the stabilization of *NO on Fe-MoS$_2$ enhances the catalytic activity – in agreement with the Brønsted–Evans–Polanyi (BEP) relation that has been proposed to describe multi-step processes (see Supplementary Information). To visualize the bonding situations between the active site and the N atom of NO, we employed the Crystal Orbital Hamiltonian Populations (COHP) analysis,[60,61] which is a theoretical method for partitioning the band-structure energy into orbital-pair interactions. The integrated projected COHP (IpCOHP) below the Fermi level

provides qualitative estimation of the bond strength. Usually, the bonding state is characterized by a positive overlap population that leads to negative Hamiltonian off-site elements that contribute to increasing the interactions between adsorbates and the catalyst surface. A comparison of the COHP curves for the four different catalysts (as seen in **Figure 4e**) reveals that a significant number of antibonding states of M-N interactions (with M and N being the transition metal atom and the N atom in NO) are below the Fermi level of the Ni-MoS$_2$ and Cu-MoS$_2$. Conversely, fewer antibonding states of M-N are present below the Fermi levels of the Fe-MoS$_2$ and Co-MoS$_2$, which indicates that there is a larger orbital overlap between the d band of the catalyst and the 2π* of *NO and a lower electron density in the antibonding orbitals below the Fermi level in both Fe-MoS$_2$ and the Co-MoS$_2$. The IpCOHP between Fe and N for Fe-MoS$_2$ was found to be -2.74 eV more negative than the other three MoS$_2$ SACs suggesting that stabilization of *NO intermediate is responsible for the reduction of the barrier for the formation of the *N intermediate associated with the PDS step of the reaction.

Solar-driven NO$_3$RR

To evaluate the potential of Fe-MoS$_2$ for practical ammonia production devices, we integrated the catalysts in a two-electrode H-cell reactor powered by an external photovoltaic (PV) cell. **Figure 5a** shows the respective polarization curves of the cathode and the anode measured in a 3-electrode configuration. The onset potentials for the NO$_3$RR and OER – measured by definition at 1 mA cm^2 were estimated to be -0.13 V and 2.06 V vs. RHE, respectively, giving an onset potential of 2.2 V for the full cell. **Figure 5b** presents the electrocatalytic response of the electrolyzer for applied potentials between 0 to 5.0 without compensating for internal resistance. The 2-electrode electrolyzer exhibited an onset potential of 2.26 V consistent with the value predicted from our 3-electrode experiments. We then evaluated the electrolysis property of the full cell, while the Faradaic efficiency was systematically measured at increasing cell voltage. The Faradaic efficiency for NH$_3$

continuously increased up to 4 V to approach a near-unity value. **Figure 5c,d** summarize the full cell energy efficiency (EE), the yield rate, EPC, and the electric power consumption (EPC, in kWh kg^{-1})obtained by varying the voltage. The EE$_{full-cell}$ was estimated to be 24.2 %, which indicates that our Fe-MoS$_2$ nanosheets possess a high conversion capability from electric to chemical energy. In addition, the EPC was found to be 46.6 kWh kg^{-1} at 4.0 V while the yield rate reaches a value of 0.024 mmol h^{-1} cm^{-2} equivalent to 412.6 µg h^{-1} cm^{-2}. We coupled the 2-electrode H-cell reactor with a PV cell to achieve indirect photocatalytic conversion of nitrate to ammonia. The relatively large potential associated with the electrochemical synthesis of ammonia typically makes the combination of PV and electrolysis processes difficult to realize experimentally at reasonable efficiencies. A GaInAs/Ga(In)As/Ge triple-junction solar cell was used to generate sufficient photovoltage to drive the catalytic reaction. As presented in **Figure 5d** and **Supplementary Figure 18**, the negative and positive poles were connected with wires to the Fe-MoS$_2$ cathode and Pt anodes, respectively, and the solar cell was illuminated by standard AM 1.5G spectrum (100 mW cm^{-2}) provided by a Xe solar simulator. **Figure 5e** presents the J–V characteristic curve of the tandem cell under 1 sun, yielding a V_{OC} of ≈ 5 V while exhibiting a solar-to-electric power conversion efficiency (PCE) of 29.89 %. To accurately calculate the solar-to-ammonia (STA) conversion efficiency, the LSV curve of the full cell was measured. The size of the electrodes was adjusted in order to minimize the energy loss of the PV-driven electrolysis. We estimated the energy loss between the PV and the PV-electrolysis systems to be only 4.25 % (**Supplementary Figure 19**). The operating point was determined from the intersection of the J–V curves of both the solar cell and the H-cell reactor.[62] The results show that the current density and the cell tension at the operating point reached ~ 7.19 mA cm^{-2} and 4.02 V respectively as shown by the red point in **Figure 5e**. Using the thermodynamic potential of the reaction, the electrolysis current, and the Faradaic efficiency (See Supplementary information for details about the calculations), we estimated the STA

348 efficiency to be ~3.9 %. To confirm the accuracy of the predicted operating point, we also

349 measured the photocurrents from the NO$_3$RR process in an unbiased light-driven configuration

350 (**Figure 5f**). The operating point of the NO$_3$RR was close to the maximum power point (MPP)

351 of the solar panel tandem cell (7.06 mA cm^{-2} at V$_{MP}$=4.23 V) (the orange point in **Figure 5e**).

352 We performed solar-driven electrolysis of nitrate for 1 hour and the amount of NH$_3$ was

353 estimated to reach 60.7 µmol; equivalent to a concentration of 1.02 mM or 17.3 ppm – larger

354 the contamination threshold of $\approx$ 1 ppm.[12] The phototcatalytic acivity corresponds to a yield

355 rate of ~ 0.03 mmol h^{-1} cm^{-2}, equivalent to 510 µg h^{-1} cm^{-2}, which outperforms the previous

356 report on the photocatalysis of the NO$_3$RR (see **Supplementary Table 7**). The estimated STA

357 efficiency was found to be ~ 3.4 %. To the best of our knowledge, such a value for the STA has

358 not been previously reported and sets a new benchmark for solar-driven ammonia production.

359

CONCLUSION

361 In summary, we have designed a Fe single-atomic catalyst on two-dimensional MoS$_2$

362 nanosheets for electrocatalytic conversion of nitrate to ammonia. Fe-MoS$_2$ catalysts exhibit

363 excellent NO$_3$RR properties with Faradaic efficiency as high as 98 % for production of NH$_3$ at

364 a low overpotential of < -0.5 V *vs*. RHE and a cathodic energy efficiency of 31 % at -0.28 V *vs*.

365 RHE. The catalytic performance of Fe-MoS$_2$ towards NO$_3$RR is among the highest reported.

366 The excellent activity and selectivity of Fe-MoS$_2$ are supported by DFT analysis, which

367 confirmed the superior ability of individual Fe atoms on MoS$_2$ to activate NO$_3^-$ due to the strong

368 interaction between $2\pi^*$ orbital of NO species and *d* band orbitals of Fe atoms that leads to low

369 energy barrier for the limiting *NO to *N reaction. We integrated Fe-MoS$_2$ in a two-electrode

370 H cell reactor coupled to a PV cell and achieved a solar-to-ammonia conversion efficiency of

371 ca. 3.4 % with a yield rate of 510 µg h^{-1} cm^{-2}. Our investigation sheds light on a practical

strategy for the realization of PV-electrolysis systems for the production of ammonia and opens

up future applications for solar-driven NH_3 production.

AUTHOR INFORMATION

Corresponding Author

*E-mail: damien.voiry@umontpellier.fr. (Damien Voiry)

Notes

The authors declare no competing financial interest

ACKNOWLEDGEMENTS

400

401

402 **AUTHOR CONTRIBUTIONS**

403 D.V. conceived the idea, designed the experiments and wrote the manuscript. J.L. designed the
404 experiments with D.V., synthesize the materials, performed the electrochemical measurements
405 and the DFT calculations. J.L. and D.V. analyzed the data and wrote the manuscript. C.L. and
406 L.Z. synthesized the materials and performed the physical characterizations. E.P. carried out
407 the NRM measurements. K.Q, Z.Y., H.W. assisted J.L. with the electrochemical measurements.
408 W.W. performed the Raman spectroscopy on the samples with J.L.. X.W. and M.C. discussed
409 the data with J.L. and D.V. L.L. performed high-resolution TEM and EELS on the Fe-MoS$_2$
410 catalysts. R.Y. performed the STEM measurements. All of the authors edited the manuscript
411 before submission.

412

413 **DATA AVAILABILITY**

414 The data that support the plots within this paper and other findings of this study are available
415 from the corresponding authors upon reasonable request.

416

417 **REFERENCES**

418   1.   Rosca, V. et al. Nitrogen Cycle Electrocatalysis. *Chem. Rev.* **109**, 2209–2244 (2009).

419   2.   Guo, W. et al. Electrochemical nitrogen fixation and utilization: Theories, advanced

420   catalyst materials and system design. *Chem. Soc. Rev.* **48**, 5658–5716 (2019).

421   3.   Steffen, W. et al. Planetary boundaries: Guiding human development on a changing

422   planet. *Science (80-.).* **347** (2015).

423   4.   Schlögl, R. Catalytic Synthesis of Ammonia—A "Never-Ending Story"? *Angew.*

424   *Chemie Int. Ed.* **42**, 2004–2008 (2003).

425   5.   Fryzuk, M.D. Ammonia transformed. *Nature* **427**, 498–499 (2004).

426   6.   Guo, J. et al. Catalyst: NH3 as an Energy Carrier. *Chem* **3**, 709–712 (2017).

427   7.   He, C. et al. Identification of FeN4 as an Efficient Active Site for Electrochemical N2

428   Reduction. *ACS Catal.* **9**, 7311–7317 (2019).

429   8.   Chen, X. et al. Photocatalytic fixation of nitrogen to ammonia: state-of-the-art

430   advancements and future prospects. *Mater. Horizons* **5**, 9–27 (2018).

431   9.   Rafiqul, I. et al. Energy efficiency improvements in ammonia production—

432   perspectives and uncertainties. *Energy* **30**, 2487–2504 (2005).

433   10. Bao, D. et al. Electrochemical Reduction of N 2 under Ambient Conditions for

434   Artificial N 2 Fixation and Renewable Energy Storage Using N 2 /NH 3 Cycle. *Adv.*

435   *Mater.* **29**, 1–5 (2017).

436   11. Luo, Y. et al. Efficient Electrocatalytic N 2 Fixation with MXene under Ambient

437   Conditions. *Joule* **3**, 279–289 (2019).

438   12. Andersen, S.Z. et al. A rigorous electrochemical ammonia synthesis protocol with

439   quantitative isotope measurements. *Nature* **570**, 504–508 (2019).

440   13. Shi, R. et al. Defect Engineering in Photocatalytic Nitrogen Fixation. *ACS Catal.* **9**,

441   9739–9750 (2019).

442   14. Qin, Q. et al. Single-Site Gold Catalysts on Hierarchical N-Doped Porous Noble

443   Carbon for Enhanced Electrochemical Reduction of Nitrogen. *Small Methods* **2**,

444   1800202 (2018).

445   15.   Zhang, J. et al. Adsorbing and Activating N 2 on Heterogeneous Au–Fe 3 O 4

446   Nanoparticles for N 2 Fixation. *Adv. Funct. Mater.* **30**, 1906579 (2020).

447   16.   Zeng, L. et al. Highly boosted gas diffusion for enhanced electrocatalytic reduction of

448   N 2 to NH 3 on 3D hollow Co–MoS 2 nanostructures. *Nanoscale* **12**, 6029–6036

449   (2020).

450   17.   Chen, G.-F. et al. Electrochemical reduction of nitrate to ammonia via direct eight-

451   electron transfer using a copper–molecular solid catalyst. *Nat. Energy* **5**, 605–613

452   (2020).

453   18.   Stirling, A. et al. Density functional study of nitrogen oxides. *J. Chem. Phys.* **100**,

454   2910–2923 (1994).

455   19.   Rai, R.K. et al. Room-Temperature Catalytic Reduction of Aqueous Nitrate to

456   Ammonia with Ni Nanoparticles Immobilized on an Fe 3 O 4 @n-SiO 2 @h-SiO 2 -

457   NH 2 Support. *Eur. J. Inorg. Chem.* **2017**, 2450–2456 (2017).

458   20.   Xu, S. et al. A flexible, redox-active macrocycle enables the electrocatalytic reduction

459   of nitrate to ammonia by a cobalt complex. *Chem. Sci.* **9**, 4950–4958 (2018).

460   21.   Li, W. et al. Electrochemical Reduction of High-Concentrated Nitrate Using Ti/TiO2

461   Nanotube Array Anode and Fe Cathode in Dual-Chamber Cell. *Catal. Letters* **146**,

462   2585–2595 (2016).

463   22.   Wu, T. et al. Self-supported Cu nanosheets derived from CuCl-CuO for highly efficient

464   electrochemical degradation of NO3−. *Appl. Surf. Sci.* **489**, 321–329 (2019).

465   23.   Reyter, D. et al. Electrocatalytic reduction of nitrate on copper electrodes prepared by

466   high-energy ball milling. *J. Electroanal. Chem.* **596**, 13–24 (2006).

467   24.   Wang, Y. et al. Unveiling the Activity Origin of a Copper-based Electrocatalyst for

468   Selective Nitrate Reduction to Ammonia. *Angew. Chemie Int. Ed.* **59**, 5350–5354

469   (2020).

470   25.   Wang, Y. et al. Enhanced Nitrate-to-Ammonia Activity on Copper–Nickel Alloys via

471   Tuning of Intermediate Adsorption. *J. Am. Chem. Soc.* **142**, 5702–5708 (2020).

472   26.   Su, L. et al. Electrochemical nitrate reduction by using a novel Co 3 O 4 /Ti cathode.

473   *Water Res.* **120**, 1–11 (2017).

474   27.   Gao, J. et al. Non-precious Co3O4-TiO2/Ti cathode based electrocatalytic nitrate

475   reduction: Preparation, performance and mechanism. *Appl. Catal. B Environ.* (2019).

476   28.   Li, C. et al. Electrochemical removal of nitrate using a nanosheet structured Co3O4/Ti

477   cathode: Effects of temperature, current and pH adjusting. *Sep. Purif. Technol.* **237**,

478   116485 (2020).

479   29.   Wang, Y. et al. Self-template synthesis of hierarchically structured Co3O4@NiO

480   bifunctional electrodes for selective nitrate reduction and tetrahydroisoquinolines semi-

481   dehydrogenation. *Sci. China Mater.* **63**, 2530–2538 (2020).

482   30.   Ghazouani, M. et al. Efficiency of electrochemical denitrification using electrolysis cell

483   containing BDD electrode. *Desalin. Water Treat.*, 1–11 (2014).

484   31.   Ding, J. et al. Electroreduction of nitrate in water: Role of cathode and cell

485   configuration. *Chem. Eng. J.* **271**, 252–259 (2015).

486   32.   Maachou, L. et al. Biomimetic electro-oxidation of alkyl sulfides from exfoliated

487   molybdenum disulfide nanosheets. *J. Mater. Chem. A* **8**, 25053–25060 (2020).

488   33.   Teng, W. et al. Selective Nitrate Reduction to Dinitrogen by Electrocatalysis on

489   Nanoscale Iron Encapsulated in Mesoporous Carbon. *Environ. Sci. Technol.* **52**, 230–

490   236 (2018).

491   34.   You, G. et al. Effects of zero valent iron on nitrate removal in anaerobic bioreactor

492   with various carbon-to-nitrate ratios: Bio-electrochemical properties, energy regulation

493   strategies and biological response mechanisms. *Chem. Eng. J.* **419**, 129646 (2021).

494   35. Liu, Z. et al. Electrochemically mediated nitrate reduction on nanoconfined zerovalent

495   iron: Properties and mechanism. *Water Res.* **173**, 115596 (2020).

496   36. He, B.L. et al. Iron-embedded C 2 N monolayer: a promising low-cost and high-

497   activity single-atom catalyst for CO oxidation. *Phys. Chem. Chem. Phys.* **18**, 24261–

498   24269 (2016).

499   37. Liu, D. et al. 2D Single-Atom Catalyst with Optimized Iron Sites Produced by Thermal

500   Melting of Metal–Organic Frameworks for Oxygen Reduction Reaction. *Small*

501   *Methods* **4**, 1900827 (2020).

502   38. Zhu, C. et al. Hierarchically Porous M-N-C (M = Co and Fe) Single-Atom

503   Electrocatalysts with Robust MN x Active Moieties Enable Enhanced ORR

504   Performance. *Adv. Energy Mater.* **8**, 1801956 (2018).

505   39. Xiao, M. et al. Microporous Framework Induced Synthesis of Single-Atom Dispersed

506   Fe-N-C Acidic ORR Catalyst and Its in Situ Reduced Fe-N 4 Active Site Identification

507   Revealed by X-ray Absorption Spectroscopy. *ACS Catal.* **8**, 2824–2832 (2018).

508   40. Zhang, H. et al. A Graphene-Supported Single-Atom FeN 5 Catalytic Site for Efficient

509   Electrochemical CO 2 Reduction. *Angew. Chemie Int. Ed.* **58**, 14871–14876 (2019).

510   41. Vijay, S. et al. Dipole-Field Interactions Determine the CO 2 Reduction Activity of 2D

511   Fe–N–C Single-Atom Catalysts. *ACS Catal.* **10**, 7826–7835 (2020).

512   42. Lü, F. et al. Nitrogen-coordinated single Fe sites for efficient electrocatalytic N2

513   fixation in neutral media. *Nano Energy* **61**, 420–427 (2019).

514   43. Zhang, L. et al. A Janus Fe-SnO 2 Catalyst that Enables Bifunctional Electrochemical

515   Nitrogen Fixation. *Angew. Chemie* **132**, 10980–10985 (2020).

516   44. Zhang, L. et al. Electrochemical Ammonia Synthesis via Nitrogen Reduction Reaction

517   on a MoS 2 Catalyst: Theoretical and Experimental Studies. *Adv. Mater.* **30**, 1800191

518   (2018).

519   45.   Yang, J. et al. Ultrahigh-current-density niobium disulfide catalysts for hydrogen

520   evolution. *Nat. Mater.* **18**, 1309–1314 (2019).

521   46.   Tang, B. et al. Simultaneous edge and electronic control of MoS 2 nanosheets through

522   Fe doping for an efficient oxygen evolution reaction. *Nanoscale* **10**, 20113–20119

523   (2018).

524   47.   Li, M. et al. Scalable Dry Production Process of a Superior 3D Net-Like Carbon-Based

525   Iron Oxide Anode Material for Lithium-Ion Batteries. *Angew. Chemie* **129**, 12823–

526   12827 (2017).

527   48.   Chen, X. et al. Functionalization of Two-Dimensional MoS 2 : On the Reaction

528   Between MoS 2 and Organic Thiols. *Angew. Chemie Int. Ed.* **55**, 5803–5808 (2016).

529   49.   Shi, Y. et al. Self-assembly of hierarchical MoS x /CNT nanocomposites (2,x,3):

530   towards high performance anode materials for lithium ion batteries.(2013).

531   50.   Wang, R. et al. FeS 2 Nanoparticles Decorated Graphene as Microbial-Fuel-Cell

532   Anode Achieving High Power Density. *Adv. Mater.* **30**, 1800618 (2018).

533   51.   Wang, Y. et al. Enhanced Nitrate-to-Ammonia Activity on Copper-Nickel Alloys via

534   Tuning of Intermediate Adsorption. *J. Am. Chem. Soc.* (2020).

535   52.   Fu, X. et al. Alternative route for electrochemical ammonia synthesis by reduction of

536   nitrate on copper nanosheets. *Appl. Mater. Today* (2020).

537   53.   Wang, Y. et al. Unveiling the Activity Origin of a Copper-based Electrocatalyst for

538   Selective Nitrate Reduction to Ammonia. *Angew. Chemie - Int. Ed.* **59**, 5350–5354

539   (2020).

540   54.   McEnaney, J.M. et al. Electrolyte engineering for efficient electrochemical nitrate

541   reduction to ammonia on a titanium electrode. *ACS Sustain. Chem. Eng.* (2020).

542   55.   Chen, G.F. et al. Electrochemical reduction of nitrate to ammonia via direct eight-

543   electron transfer using a copper–molecular solid catalyst. *Nat. Energy* (2020).

544   56.   Dubouis, N. et al. Interfacial Interactions as an Electrochemical Tool To Understand

545   Mo-Based Catalysts for the Hydrogen Evolution Reaction. *ACS Catal.* **8**, 828–836

546   (2018).

547   57.   Yang, T. et al. High-throughput screening of transition metal single atom catalysts

548   anchored on molybdenum disulfide for nitrogen fixation. *Nano Energy* **68**, 104304

549   (2020).

550   58.   Liu, J.-X. et al. Activity and Selectivity Trends in Electrocatalytic Nitrate Reduction on

551   Transition Metals. *ACS Catal.* **9**, 7052–7064 (2019).

552   59.   Li, G. et al. All The Catalytic Active Sites of MoS 2 for Hydrogen Evolution. *J. Am.*

553   *Chem. Soc.* **138**, 16632–16638 (2016).

554   60.   Dronskowski, R. et al. Crystal orbital hamilton populations (COHP). Energy-resolved

555   visualization of chemical bonding in solids based on density-functional calculations. *J.*

556   *Phys. Chem.* **97**, 8617–8624 (1993).

557   61.   Nelson, R. et al. LOBSTER: Local orbital projections, atomic charges, and chemical-

558   bonding analysis from projector-augmented-wave-based density-functional theory. *J.*

559   *Comput. Chem.* **41**, 1931–1940 (2020).

560   62.   Jingshan, L. et al. Water Photolysis at 12.3% Efficiency Via Perovskite Photovoltaics

561   and Earth-Abundant Catalysts. *Science (80-.).* (2014).

562

563
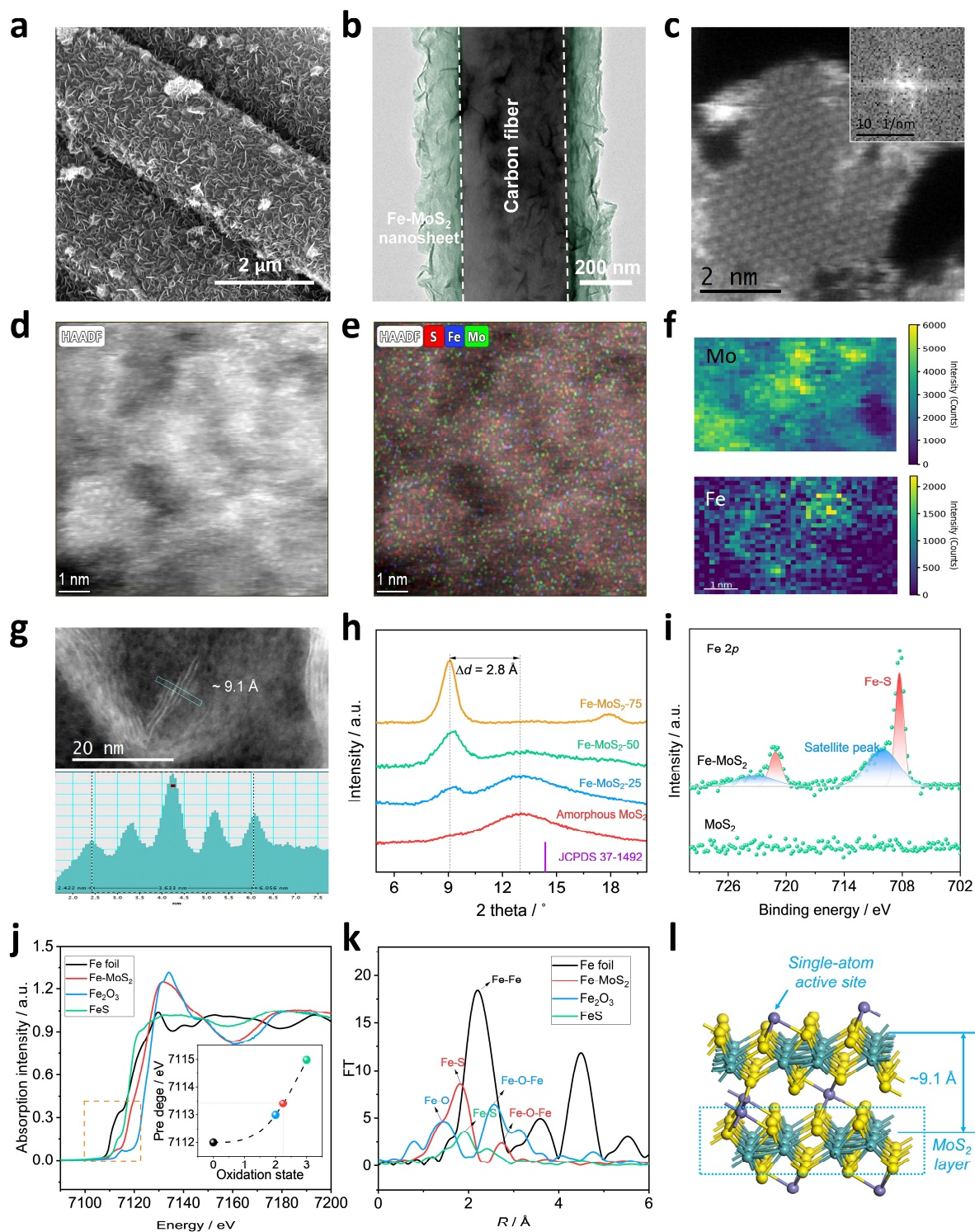
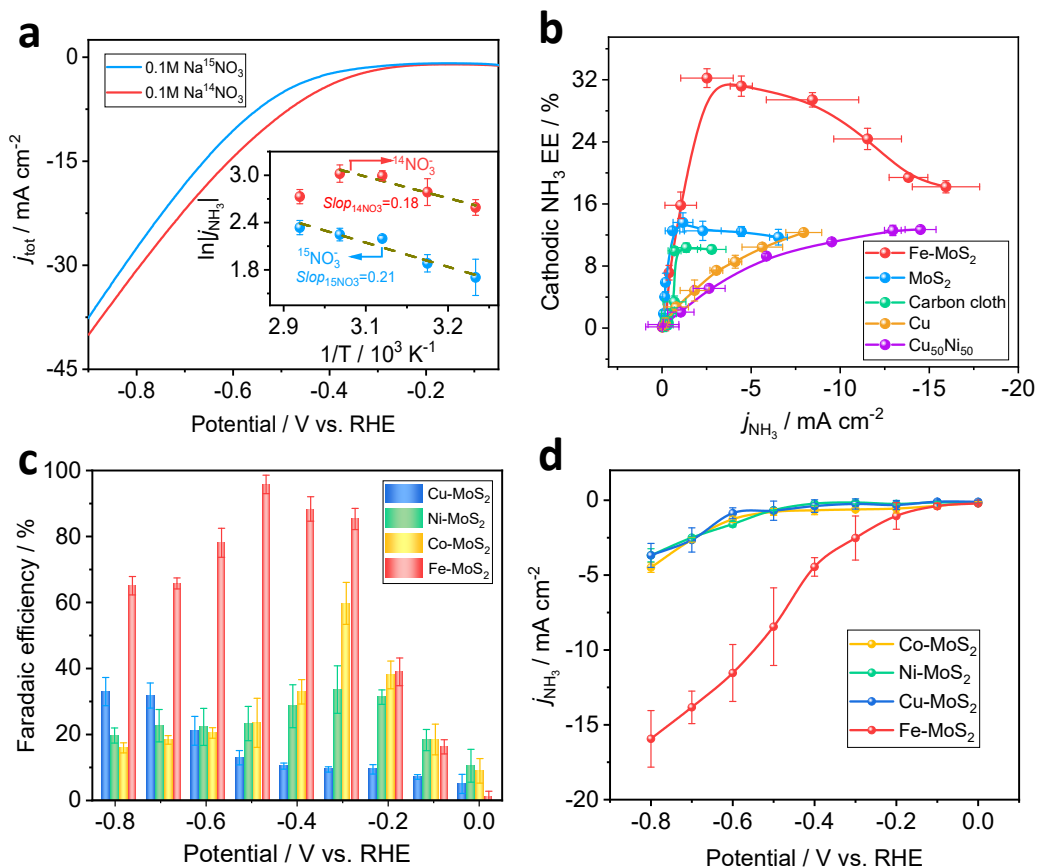**FIGURES**

Figure 1 | The physical characterizations of Fe-MoS₂. a,b, Scanning electron microscopy (SEM) and transmission electron microscopy (TEM) images of the Fe-MoS₂ nanosheets grown on the carbon support. **c,d,** High-angle annular dark-field imaging scanning transmission electron microscopy (HAADF-STEM) image of Fe-MoS₂ nanosheets. Inset: corresponding

570   diffraction pattern confirming the single-crystalline nature of the nanosheet. **e,f**, High resolution

571   TEM (HRTEM) - energy dispersive X-ray analyses (EDX) and electron energy loss (EELS)

572   elemental mapping images of Fe-MoS$_2$ nanosheets. **g**, HR-STEM image of the interlayer

573   spacing of Fe-MoS$_2$ and the corresponding line profiles showing an average d-spacing of ≈ 9.1

574   Å. **h**, X-ray diffraction (XRD) patterns of the Fe-MoS$_2$ nanosheets with different iron content

575   and compared to pristine MoS$_2$. **i**, High resolution Fe2p XPS spectra for Fe-MoS$_2$ and MoS$_2$. **j**,

576   Normalized XANES spectra and **k**, Fourier transform magnitudes in *R* space of the EXAFS at

577   the Fe K edge of Fe-MoS$_2$ nanosheets, Fe$_2$O$_3$, FeS, and Fe foil, **i**, Proposed structure of Fe-

578   MoS$_2$.

579
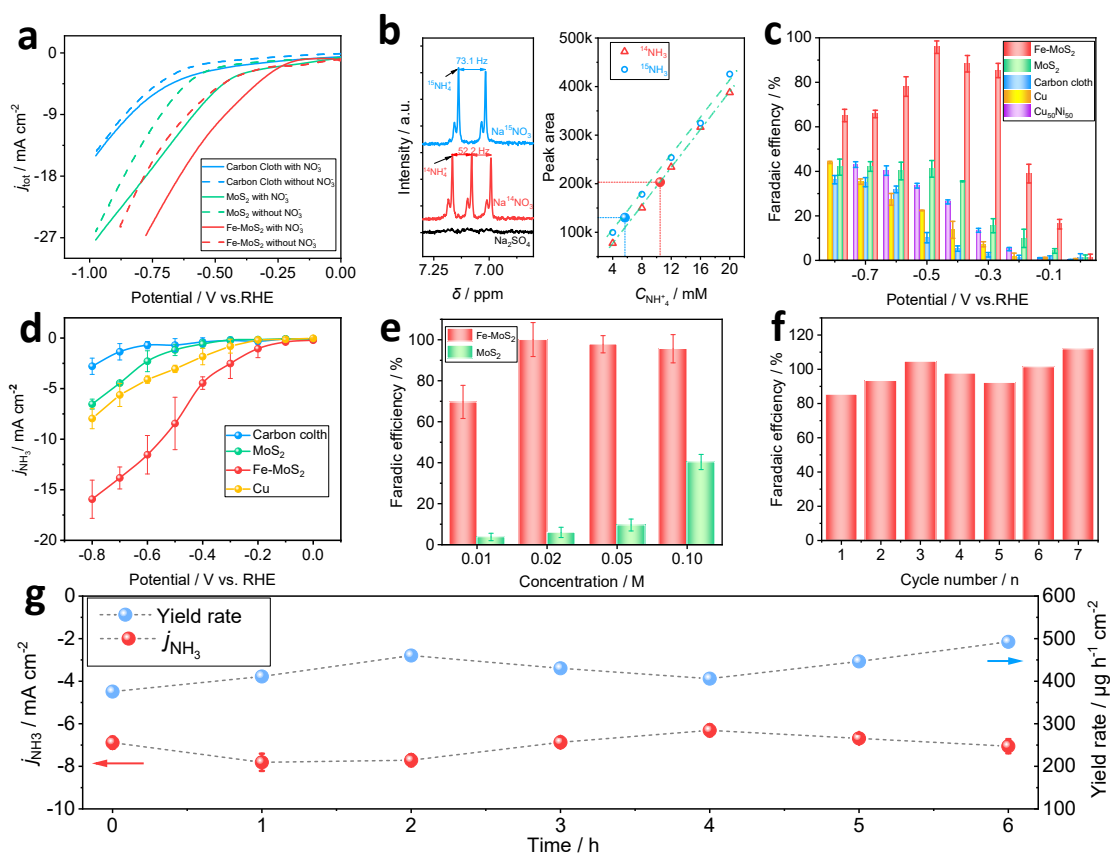
Figure 2 | The electrochemical performance investigation for NO₃RR on Fe-MoS₂. a, LSV curves of Fe-MoS₂ nanosheets, MoS₂ nanosheets, and the carbon support measured with and without 0.1 M NaNO₃ electrolyte. **b,** *Left:* ¹H nuclear magnetic resonance (NMR) spectra (600 MHz) of electrolyte produced from NO₃RR under -0.58 V vs. RHE using 0.1 M Na¹⁴NO₃ and Na¹⁵NO₃ as N source. *Right:* Calibration curve of ¹⁴NH₄Cl and ¹⁵NH₄Cl measured by ¹H NMR (right). The experimental NO₃RR results are show as solid symbols. **c,** Potential-dependent Faradaic efficiency of ammonia on Fe-MoS₂, MoS₂, Cu, Cu₅₀Ni₅₀ alloy, compared with the carbon support. **d,** Evolution of the specific current density: j_{NH3} as a function of the potential (*vs.* RHE). **e,** Comparison of the Faradic efficiency for ammonia on the Fe-MoS₂ and MoS₂ nanosheets at different nitrate concentrations measured at an applied potential of -0.48 V *vs.* RHE. **f,** Evolution of the Faradaic efficiency at -0.48 V over 7 cycles of 1 hour. The electrolyte was refreshed for every cycle. **h,** Evolution of j_{NH3} and the yield rate of Fe-MoS₂ nanosheets over time.

Figure 3 | The electrochemical performance towards NO₃RR on MoS₂-based SACs. a,
Linear scanning voltammetry (LSV) and Arrhenius plots (inset) of Fe-MoS₂ measured in
Na¹⁴NO₃ and Na¹⁵NO₃ at different temperatures. **b,** The cathodic energy efficiency (EE) for
NO_3^--to-NH₃ conversion on Fe-MoS₂ and MoS₂ nanosheets compared with Cu, Cu₅₀Ni₅₀, and
the carbon support. **c,** Potential-dependent Faradaic efficiency for ammonia on Cu-MoS₂, Ni-
MoS₂, Co-MoS₂ and Fe-MoS₂ nanosheets. **d,** Evolution of j_{NH3} on Co-MoS₂, Co-MoS₂, and Co-
MoS₂ nanosheets as a function of the applied potential.
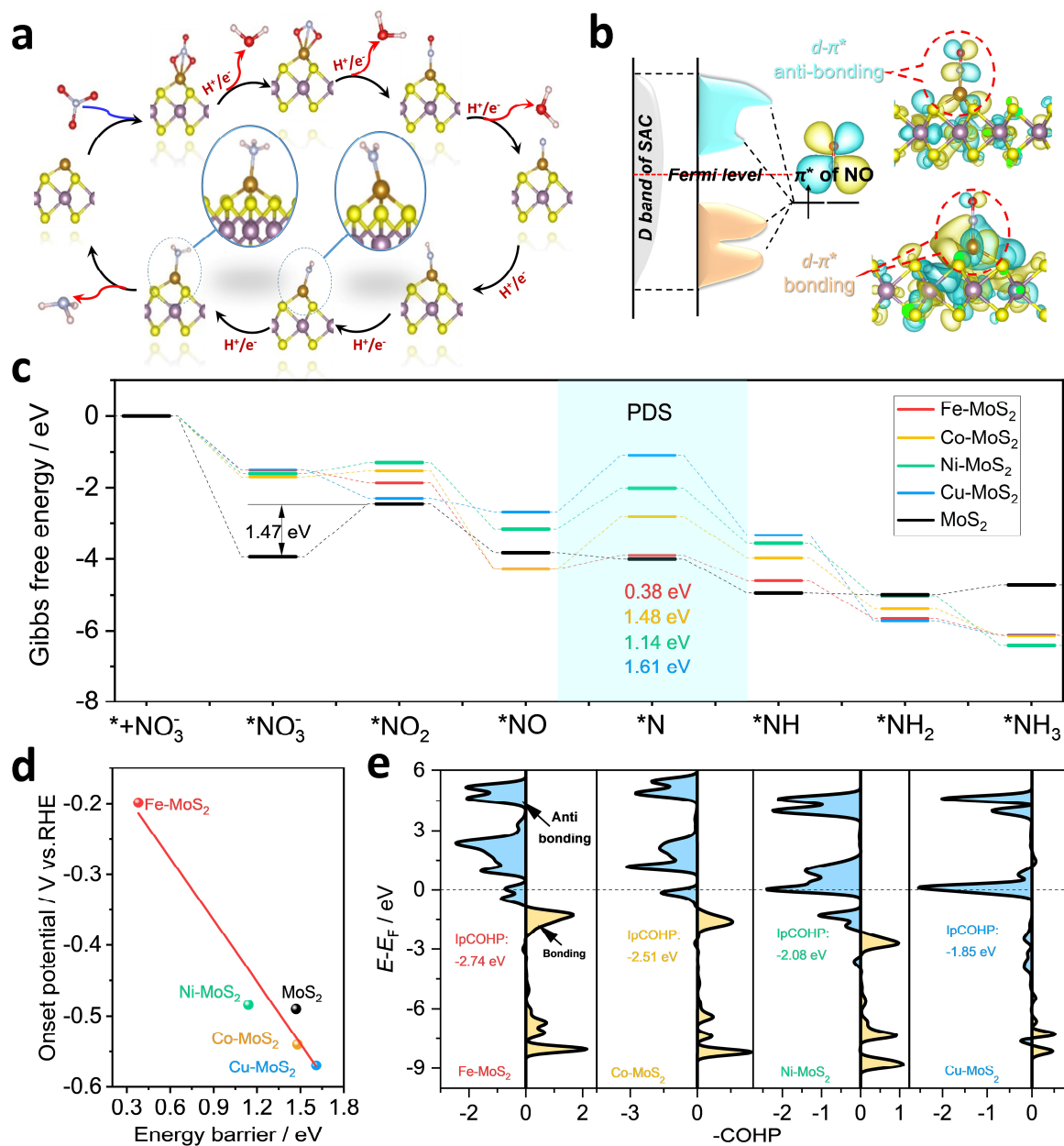
Figure 4 | DFT calculations of the NO₃RR on MoS₂ SACs. a, Reaction pathway for the NO₃RR on M-MoS₂ nanosheets (M: Fe, Co, Ni, and Cu, respectively). **b**, Schematic diagram of the interaction between NO and the M-MoS₂ nanosheets. **c**, Reaction Gibbs free energies for different intermediates on M-MoS₂ nanosheets. **d**, Scaling relationship between energy barrier and onset potential of NO₃RR for pristine MoS₂ and M-MoS₂. **e**, Projected crystal orbital Hamilton population (pCOHP) of NO adsorbed on M-MoS₂ nanosheets.

609
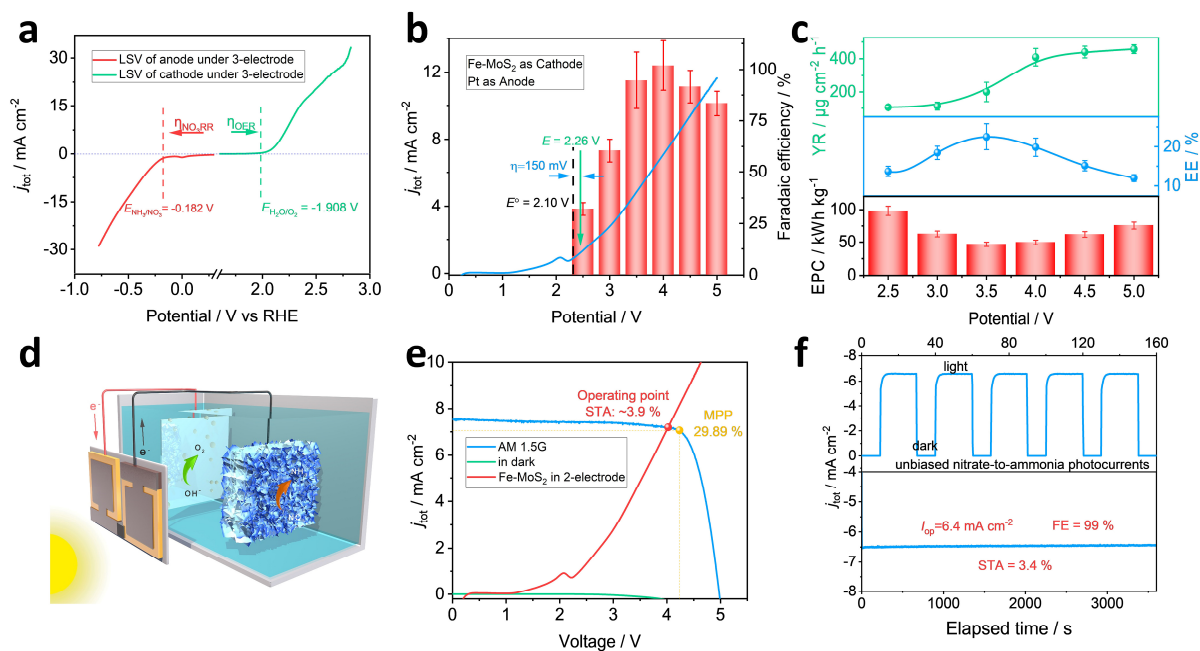
Figure 5 | The performance of Fe-MoS₂ for NO₃RR using a 2-electrode electrolyzer. a, LSV curves of Fe-MoS₂ nanosheets and Pt used as a cathode and anode. The LSV responses were measured in a 3-electrode configuration. **b**, Polarization curve of the full cell electrolyzer with a total geometric area of 2 cm². **c**, Potential-dependent electric power consumption of ammonia, yield rate, and energetic conversion efficiency of the full-cell device. **d**, Schematic of the photovoltaic-electrolysis system for the conversion of nitrate to ammonia. **e**, *J*–V characteristics of the triple junction solar under dark and simulated AM 1.5G 100 mW cm⁻² illumination. Polarization curves of the full cell device based on Fe-MoS₂ nanosheets as NO₃RR catalyst at the cathode. **f**, *Top:* Current density–time curve of the PV-EC system without external bias under chopped simulated AM 1.5G 100 mW cm⁻² illumination. *Bottom:* Stability of the photocatalytic current over 1 hour.

621

29

Supplementary Files

This is a list of supplementary files associated with this preprint. Click to download.

- NO3RRESIV9Ji.pdf